Materials Science & Engineering A 844 (2022) 143191

Contents lists available at ScienceDirect

Materials Science & Engineering A

journal homepage: www.elsevier.com/locate/msea

Influence of DIMT on impact toughness: Relationship between crack propagation and the α′-martensite morphology in austenitic steel

Minghao Huang [a], Chenchong Wang [a], Lingyu Wang [a,**], Jinliang Wang [b], Anna Mogucheva [c], Wei Xu [a,*]

[a] State Key Laboratory of Rolling and Automation, School of Materials Science and Engineering, Northeastern University, Shenyang, 110819, China
[b] School of Mechanical and Power Engineering, Guangdong Ocean University, Zhanjiang, 524000, China
[c] Laboratory of Mechanical Properties of Nanoscale Materials and Superalloys, Belgorod State University, Belgorod, 308015, Russia

ARTICLE INFO

Keywords:
α′-martensite morphology
Crack propagation
Grain size
Austenitic steel
Deformation-induced martensitic transformation

ABSTRACT

The trade-off between transformation-induced plasticity (TRIP) strengthening and the intrinsically brittle nature of deformation-induced α′-martensite (DIM) has been a long-standing dilemma in optimizing the strength–toughness synergy of austenitic steels. This has limited their potential use, particularly in energy absorption applications. Here, we propose a new strategy to minimize the negative effect of intrinsically brittle α′-martensite without limiting the TRIP. In this study, austenitic 321 stainless steel samples with different austenite grain sizes (AGSs) were fabricated to tailor the DIM morphology. The effect of the DIM morphology on the crack propagation energy was simultaneously evaluated. Electron channeling contrast imaging (ECCI) and selected area electron backscattered diffraction (EBSD) of the Charpy fractures reveals that lath-like α′-martensite effectively deflects cracks and increases the crack propagation energy (E_p). As a consequence, coarse-grained and ultra-coarse-grained (CG/UCG) steels with lath-like α′-martensite can simultaneously achieve high strength and crack propagation resistance, while ultra-fine-grained (UFG) steel with blocky DIM exhibits the lowest E_p. Furthermore, the morphology of DIM is controlled by its nucleation sites and adjacent crystallographic/phase boundaries. The twins or ε-γ boundaries promote the formation of lath-like α′-martensite. The γ→ε→α′ transformation sequence can be explained by the change in stacking fault energy (SFE), which provides further guidance for the design of austenitic steels with high strength and high toughness.

1. Introduction

Austenitic steels with high impact toughness are ideal candidates for energy absorption applications, such as liquefied natural gas (LNG) tanks [1], pressure vessels [2], and offshore structures [3–5]. However, for safety-critical applications, their lower yield strength has limited the widespread use of austenitic steels in these applications [6]. However, the development of high-strength steels has traditionally involved a trade-off between strength and toughness [6]. With the increasing demand for steels with combined high strength and toughness, optimizing the microstructure of austenitic steels to achieve strength-toughness synergy has drawn significant attention in the past few years.

In the case of mechanical strength, previous studies have shown that deformation-induced martensitic transformation (DIMT) results in the transformation-induced plasticity (TRIP) effect which can provide significant strengthening [7–13]. Aiming to further increase the strain-hardening rate (SHR) of the alloys, considerable effort has been focused on the optimization of the TRIP effect. The first and most common is to change the alloy chemistry. Min et al. [14] demonstrated a positive relationship between the deformation-induced α′-martensite volume fraction and strength. Specifically, an increase of ~20 vol% α′-martensite led to a rise of ~200 MPa in strength. In addition to alloying methods, service temperature was also used to tailor the kinetics of DIMT [15]. As the temperature decreased from 60 °C to −40 °C, the volume fraction of the deformation induced martensite increased continuously from 0 to 75 vol%, resulting in a considerable increase in strength (from 700 to 1100 MPa). Therefore, the strength of austenitic steel is closely related to the amount of deformation martensite formed during loading.

The total Charpy impact energy (E_t) can be divided into two parts:

* Corresponding author.
** Corresponding author.
E-mail addresses: wanglingyu@ral.neu.edu.cn (L. Wang), xuwei@ral.neu.edu.cn (W. Xu).

https://doi.org/10.1016/j.msea.2022.143191
Received 8 December 2021; Received in revised form 19 March 2022; Accepted 19 April 2022
Available online 26 April 2022

the energy for crack initiation (E_i) and the energy consumed by crack propagation (E_p). The high strain rates during the Charpy impact tests (10^2–10^3 s^{-1}) make it hard to study the effect of DIMT on E_i. Thus, the relationship between the E_p and DIMT has been the main focus of previous studies [16,17], and it is often found that the decrease in deformation-induced ε/α′-martensite (DIM) results in an increase in E_p [18–21]. In austenitic steels, the negative impact of DIM on toughness [22,23] demonstrates that the brittle DIMT products are the source of cracks or fast crack propagation in martensite or the martensite/austenite interface [24,25]. As a consequence, various studies have focused on microstructural development that suppresses the formation of ε-martensite and α′-martensite and improves E_p and E_t. For example, Kim et al. [26] and Lee et al. [27,28] studied the impact toughness of high-Mn austenitic steels with different Mn contents. An increase in the martensite (ε/α′) volume fraction led to a decreased Charpy impact energy. Based on experimental results, Antolovich et al. and Zhang et al. [29–31] proposed models to describe the quantitative relationship between the martensite phase fraction and toughness. Their models provided preliminary guidance for the design of high-toughness austenitic steels. Generally, a decreased volume fraction of DIMT products (ε-martensite/α′-martensite) leads to an increased toughness.

In this regard, the martensitic transformation behavior has two opposing effects on the strength and impact toughness: TRIP increases the strength, while the brittle DIMT products (both α′-martensite and ε-martensite) decrease the toughness [23,24]. To achieve high strength and high toughness, an optimized DIMT behavior is required. Two feasible strategies have been used to address these mutually exclusive problems. The most common is to suppress the DIMT process, thereby ensuring an ideal toughness and then achieving additional strengthening by back stress hardening [32], and twinning-induced plasticity (TWIP) [33]. However, limiting DIMT usually needs a high weight percent of an alloying element (Ni, Mn, etc.), which unfavorably increases the cost. The second method is more promising, without limiting the TRIP behavior while weakening the negative influence of the DIMT product on the impact toughness. Thus, it is necessary to systematically evaluate the internal relationship between the DIMT products and E_p.

Tailoring the austenite grain size (AGS) is considered an effective method to control the DIMT product without changing the alloy chemistry. Tiamiyu et al. [34] and Huang et al. [35] studied austenitic stainless steels with various grain sizes and found that the grain size significantly affected the morphology of DIM under dynamic loading tests. The coarse austenite grain size resulted in the increase of the aspect ratio of α′-martensite. The change in α′-martensite morphology is attributed to the martensitic transformation sequence, which influences the boundaries that limit the growth of α′-martensite [35]. In the case of mechanical properties, Matsuoka et al. [34] reported that coarse grains with lath-like α′-martensite exhibit highly desired working hardening. Kwon et al. [36] also believed that lath martensite significantly contributed to strengthening. In this study, austenitic steel samples with different grain sizes are fabricated to tailor the DIMT products after Charpy impact loading. Based on the microstructural investigation of the fracture surface, the relationship between the DIM morphology and Charpy crack propagation path is revealed.

2. Experimental work

2.1. Materials and test specimens

The material studied in this work was supplied as SUS 321 austenitic stainless steel plates with a thickness of 12 mm. The chemical composition of the austenitic stainless steel is shown in Table 1. To obtain different grain sizes, different cold rolling and annealing processes were conducted. Multi-pass cold rolling was performed to 60% reduction at room temperature. The cold-rolled specimens were subsequently annealed with various temperatures and times: 900 °C for 90 s, 900 °C for 30 min, 1000 °C for 2 h, and 1100 °C for 2 h. Sub-sized Charpy impact specimens used in the present study were 3 mm thick, 10 mm wide, and 55 mm long and were machined along the rolling direction of the cold-rolled sheets.

2.2. Microstructural and mechanical characterization

The microstructures of the specimen were observed by scanning electron microscopy (SEM) using a field-emission scanning electron microscope (GeminiSEM 300) equipped with an electron backscattered diffractometer (EBSD; Oxford Instruments NordlysNano). The EBSD results were processed using an Oxford Instruments AZtecCrystal 2.0 EBSD software. After the Charpy tests, microstructures near the cracks were observed by EBSD and electron channeling contrast imaging (ECCI). ECCI was performed using a solid-state four-quadrant backscattered electron (BSE) detector at an accelerating voltage of 30 kV and a probe current of 10 nA. Microbeam X-ray diffraction (XRD; SmartLab9KW with Cu Kα radiation, Rigaku Corporation) tests were used to determine the volume fraction of α′-martensite after the Charpy tests. In detail, a flow chart that shows the characterization process and characterization region of microbeam XRD is shown in Fig. 1. The phase volume fraction based on the microbeam XRD results was calculated based on the review of Mirzadeh et al. [37]. The specimens used for XRD, ECCI, and EBSD observation were lightly ground with sandpaper and then electropolished at 20 V for 20 s in a mixture of 700 ml glacial acetic acid (CH3COOH) and 100 ml perchloric acid (HClO4).

Charpy impact tests were performed on the SANS ZBC2452-C impact tester. The load-deflection curves were obtained in accordance with the GBT 229–2007 standard. Tensile tests were performed at room temperature with a nominal strain rate of 1×10^{-3} s^{-1} using a Shimadzu AG-X tensile machine. Three specimens were tested for each heat treatment condition, and the mean and standard deviation of the

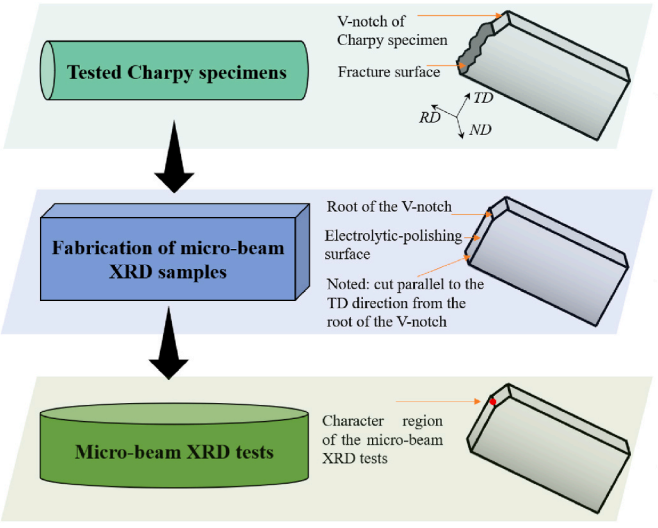

Fig. 1. Schematic diagram of the microbeam XRD test flow.

Table 1
Chemical composition (wt.%).

C	Si	Mn	Cr	P	S	Ni	N	Ti	Fe
0.021	0.578	1.384	17.56	0.033	0.0004	9.337	0.004	0.252	Balance

mechanical properties were reported.

3. Results

3.1. Microstructure of the specimens with various AGSs

Fig. 2(a–d) shows inverse-pole-figure (IPF) maps that include grain boundaries (black line) with misorientation angles (θ) > 15°. The AGS of each specimen is presented in Fig. 2(e). Specimens with AGSs of 2.2 μm, 31 μm, 72 μm, and 129 μm were obtained by annealing at 900 °C for 90 s, 900 °C for 30 min, 1000 °C for 2 h, and 1100 °C for 2 h, respectively. For clarity, specimens with AGSs of ~2.2 μm, ~31 μm, ~72 μm, and ~129 μm are referred to as ultrafine-grained (UFG), fine-grained (FG), coarse-grained (CG) specimens, and ultra-coarse-grained (UCG) specimens, respectively.

3.2. Mechanical properties of the specimens with various AGSs

The tensile behavior of the four specimens with different grain sizes investigated in this study is shown in Fig. 3(a), and the mechanical properties are summarized in Table 2. Grain size has a significant influence on the yield strength of steel, which is clearly seen in the Hall–Petch relationships [38]. The yield strength (YS) increases with decreasing grain size. The total elongation (TEL) decreases with decreasing grain size. Tensile strength is mainly governed by the strain hardening capability of the material after yielding. In the case of 321 stainless steels, strengthening can be achieved by enhancing the martensitic transformation. To obtain increasing tensile strength and uniform elongation, the maximum point in the work-hardening curve should reach an appropriate strain [37,39–41]. The change in the strength and ductility can be explained with the strain hardening rate-true strain plot shown in Fig. 3(b). It is seen that the strain hardening behavior of the UFG sample is very different to the samples with coarser grains. It consists of an increase in strain hardening up to 2–3% strain and then a shaper decrease compared to the other samples. Based on the reviews of Chen et al. [40] and Mirzadeh et al. [37,41], the higher strain hardening capability in the beginning and shaper decrease can be attributed to the faster TRIP kinetics when the grain size in austenic steel is vastly reduced. Specimens with larger grain sizes demonstrate more sustained strain hardening caused by the TRIP effect, resulting in better mechanical properties.

As discussed in the introduction, a higher YS often leads to a lower Charpy V-notch (CVN) energy [42]. Thus, the relationship between the strength parameters (both YS and UTS) and Charpy impact energy is shown in Fig. 3(c). Generally, the YS increases with the reduction in AGSs, and the Charpy impact energy decreases accordingly. In the range of UFG ~ CG with increasing AGSs, the Charpy impact energy increases correspondingly. It is worth noting that the Charpy impact energy shows limited changes when CG transitions into UCG, indicating a steady state of CVN toughness for coarse-grained austenitic steels. Therefore, the CG and UCG samples display the best strength-toughness combinations among all samples tested in this study (Fig. 3(d)).

3.3. Load–displacement curves under impact loading

It is seen that the AGS has a direct influence on the Charpy impact energy. Thus, the load (L) vs. deflection (d) curves of different grain sizes were analyzed to further understand which stage is affected the most when AGS is changed. As shown in Fig. 4(a), the overall shape of the L-d curve of the UFG steel is quite different from those of the other steels. The UFG steel possesses a relatively high dynamic YS, as seen in the peak load. After the peak load, the load immediately decreases and forms a narrow E_p region. Instead, the FG, CG and UCG samples all display a much larger E_p region. Notably, the CG and UCG steels have similar L-d curves, meaning that the AGSs in the CG-UCG region have a limited influence on the impact energy.

From the load–displacement curves, E_i and E_p were calculated by integrating the area below the curve. The initiation energy (E_i) represents the area to the left of the peak load, and the propagation energy (E_p) represents the area to the right of the peak load. The addition of E_i and E_p equals the total Charpy impact energy. As shown in Fig. 4(b), both E_i and E_p have a significant effect on the impact toughness, and the propagation energy demonstrates a more dominant effect (i.e., $E_i = 0.45\ E_t$; $E_p = 0.55\ E_t$). In the UFG-CG region, E_p increases linearly with increasing AGSs, while E_i shows a limited increase during the transition between FG and CG. Both E_p and E_i are relatively constant when the AGS coarsens further to the UCG region. These results imply that when the AGS exceeds 40 μm, a further increase in the AGS has a limited influence on the impact energy.

For 321 austenitic stainless steel, the reason why CG and UCG steel possess relatively high E_i might be attributed to the relatively low yield strength and the long-lasting working-hardening behavior before crack initiation [43]. This enables the materials to be plasticized easily before the crack is initiated. In the case of crack propagation, it is generally accepted that grain refinement would effectively improve the Charpy impact toughness and crack propagation resistance for most steels without the TRIP or the TWIP effect [44,45]. Grain refinement provides a high density of large-angle grain boundaries, which is beneficial for crack deflection. However, for austenitic steel with complex deformation behavior, crack propagation energy usually increases with the

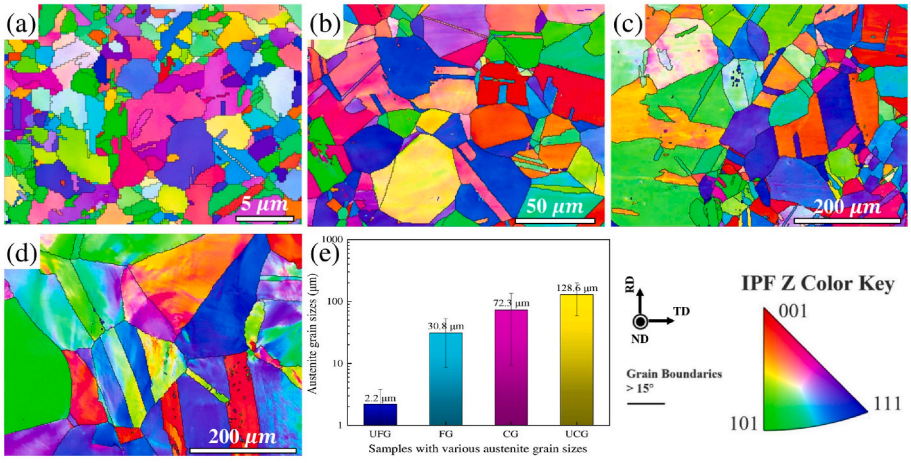

Fig. 2. SEM-EBSD IPF Z maps of specimens with (a) ultrafine grains, (b) fine grains, (c) coarse grains, and (d) ultra-coarse grains. (e) Quantified AGSs of various specimens. RD, TD, and ND represent the rolling direction, transverse direction, and normal directions, respectively.

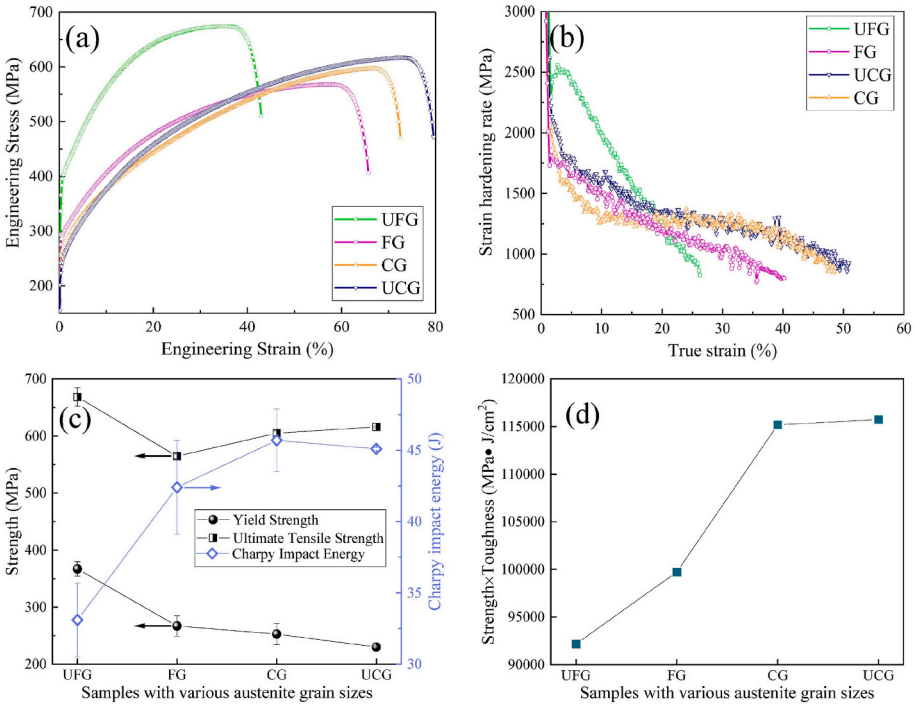

Fig. 3. (a) Engineering stress vs. strain curves, (b) strain hardening rate-true strain curves, and (c) relationship between the measured strength and Charpy impact energy of the specimens with various AGSs. (d) Product of strength and toughness change with various AGSs.

Table 2
Mechanical properties of the different specimens in this study.

Specimen	UFG steel	FG steel	CG steel	UCG steel
YS (MPa)	367.1 ± 12.8	266.9 ± 17.8	252.8 ± 18.7	229.8 ± 2.18
UTS (MPa)	668.3 ± 16.4	564.5 ± 4.3	604.9 ± 4.3	615.9 ± 1.7
Vickers hardness (HV)	261.5 ± 8.7	239.4 ± 13.4	200.3 ± 1	156.6 ± 6.3
E_t (J)	33.1 ± 2.6	42.4 ± 3.3	45.7 ± 2.2	45.1 ± 0.1

increasing grain sizes [46–49]. Wang et al. [46] claimed that the impact toughness is independent of the austenite grain size in high-Mn steel, and the crack propagation energy is related to the density of ∑3 special grain boundaries (i.e. twinning boundaries). Chen et al. [47–49] studied high-Mn austenitic steels and claimed that the high toughness of the coarse grain steel is related to the more twinning systems that occur in CG steels, which brings significant dynamic grain refinement and relatively homogeneous plastic deformation. Similar observations can be found in the present CG and UCG steels where the change in grain sizes has a minimal influence on E_p. Therefore, the superior resistance to crack propagation in CG and UCG should be attributed to the change in martensitic transformation and its transformation products, and not specifically to the change in AGS.

Since the relationship between grain size and mechanical stability confirms that larger AGSs result in less stable austenite [50,51]. The volume fraction of α′-martensite in the specimens was characterized by microbeam XRD, as shown in Fig. 4(c). In general, with increasing AGSs, the volume fraction of martensite increases. The CG and UCG steels have more DIM but a higher Charpy impact energy than the UFG/FG steel with less DIM, contradicting the statement that more DIM results in smaller E_p [22,23].

Therefore, the AGS has a complicated influence on crack propagation, which cannot be measured by the YS alone or the classical relationship between the DIMT and toughness. The CG and UCG steels exhibit unexpectedly high crack resistance, although the volume fraction of DIMT products is higher than that of the FG steel. To explain the high crack resistance (E_p) of CG and UCG steel, additional factors that influence DIMT and its sequential effect on E_p must be determined in more detail.

4. Discussion

4.1. Relationship between the α′-martensite morphology and E_p

Previous sections have shown that martensitic transformation has a complex influence on E_p. The fracture propagation energy absorbed during the Charpy impact test should be closely related to the crack propagation path. Thus, the crack propagation paths of samples with various AGSs are systematically examined in this section.

Fig. 5(a) shows the low-magnification ECCI micrographs of the cross-sectional area of a fractured Charpy impact specimen of the UFG sample. After the Charpy impact test, the UFG steel completely failed, breaking into two parts, and one side of the fractured sample is shown in Fig. 5(a). The UFG sample exhibits cracks resembling brittle fracture, the crack path is flat despite the high-density grain boundaries, and significant TRIP occurred during the impact loading. It has been reported that a high density of grain boundaries can deflect cracks and improve the impact toughness [52]. However, in the present study, the grain boundaries seem to have a weak influence on crack propagation. This brittle fracture mode is responsible for the low E_p.

Magnified graphs of the crack near the edge of the V-notch, along the middle section of the crack, and at the end of the crack are shown in Fig. 5(b), (c), and (d), respectively. Near the crack, the α′-martensite formed in the UFG steel is characterized by its globular-like shape (Fig. 5 (e) and (f)), and its fracture surface corresponds to the quasi-cleavage fracture mode. This is because the globular-like martensite hardly changes the direction of crack extension [53–56]. Regardless, the cracks propagated to nearby α′-martensite/austenite phase boundaries or through the brittle α′-martensite. Therefore, quasi-cleavage facets were induced on the fractured surface.

The crack path profile of FG steel was also carefully characterized by

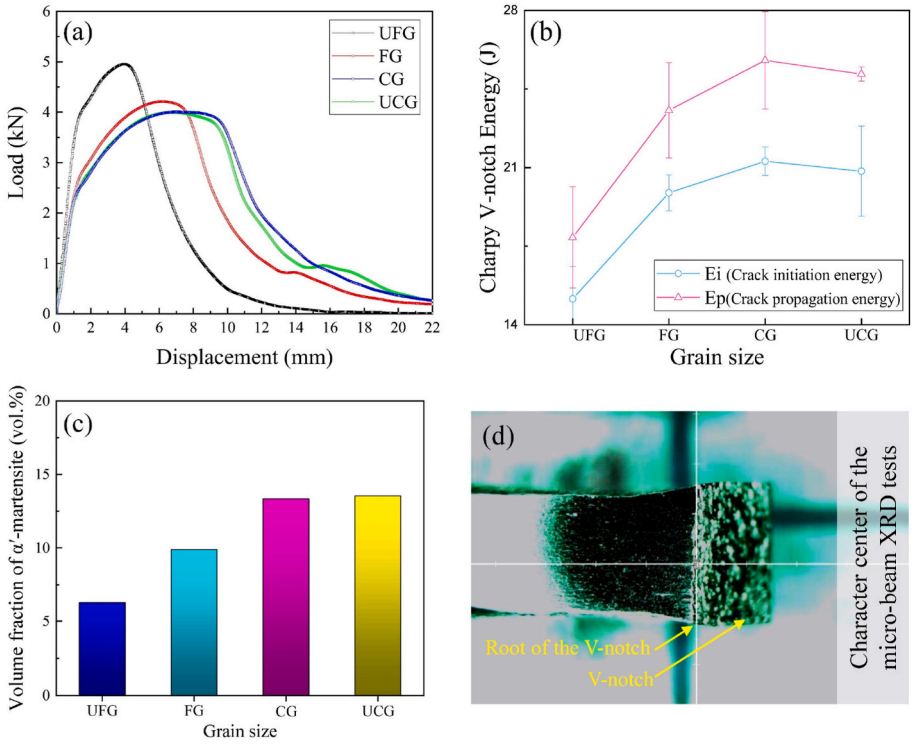

Fig. 4. (a) Load-displacement curves of the UFG, FG, CG, and UCG specimens obtained from instrumented Charpy impact tests at room temperature; (b) Impact energy results dissociated into E_i and E_p for the UFG, FG, CG, and UCG V-notched specimens; (c) Martensite phase fractions of the V-notched specimens after the Charpy test; (d) Character center of the microbeam XRD tests.

ECCI and EBSD, as shown in Fig. 6. In region a, lamellar microstructures are observed (Fig. 6(a1)). The lath-like microstructure is further identified as α′-martensite in the EBSD phase map (Fig. 6(a2)), in which red represents α′-martensite and green represents austenite. The crack propagation paths are frequently deflected due to the influence of lamellar α′-martensite, thereby forming a zig-zag pattern. In contrast, straight crack propagation is observed in region b (Fig. 6(b1)). Further characterization of the microstructure with EBSD shows that the martensite formed in this region is in the shape of large blocks (Fig. 6 (b2)), differing significantly with the one in region a. The results from crack propagation and martensite morphology indicate that the presence of blocky α′-martensite is partly responsible for the cleavage-like crack propagation path. Characterization was also carried out near the crack-tip, as shown in Fig. 6(c), in which both lath-like and blocky α′-martensite is formed in the FG sample (lamellar and blocky α′-martensite rectangles with red and blue, respectively). Generally, when cracks encounter a lamellar microstructure, the cracks are more likely to bypass it, which leads to crack deflection and a much more tortuous propagation path and higher impact energy [53–55]. It can then be concluded that the presence of a lamellar microstructure increases the toughness of high-strength steel [57].

Additionally, there are still large areas without cracks. In the uncracked region, adiabatic shear bands (ASBs) formed near the back of the specimen face, which is delineated by a red dotted line (region d). Fig. 6(d1-d3) shows the refined lamellar structures developed in the ASBs formed near the end of the band. Fig. 6(d3) identifies the lamellar structures as austenite phase. The ASBs in the FG specimen are far from the crack propagation path, which indicates that the ASBs has no impact on the crack propagation behavior. These findings reflect the insignificant role of ASBs during crack propagation, which is quite different from previous studies that suggest that ASBs are easily crossed by cracks [26].

In contrast to the FG steel, the crack propagation path of CG steel appears to be more tortuous, as shown in Fig. 7. Close to the crack path, the high-magnification ECCI images (Fig. 7(a1 and b1)) clearly show the formation of lamellar structures and the corresponding zig-zag crack propagation path. Moreover, the EBSD IPF map (Fig. 7(a2 and b2)) scanned at region-a and b (adjacent to the crack path) reveals the lamellar structures are α′-martensite. Crack propagation in the CG steel is frequently deflected by the lath-shaped α′-martensite, resulting in a more tortuous propagation path. This result is consistent with the high E_p value observed in the CG steel. Although a higher volume fraction of α′-martensite is detected in the CG steel than in the FG steel, the morphology of the lath-like α′-martensite helps deflect propagating cracks and improve its crack resistance. Note that ASBs with refined lamellar austenite are also found in the uncracked region c (Fig. 7 (c1 and c2)) The ASBs play a negligible role in influencing the crack energy, similar to the observation in the FG steel. This further confirms our view that ASBs have a negligible impact on crack propagation because the crack stops at the end of the Charpy impact process.

Similar to the CG specimen, the tested Charpy UCG specimens exhibited tortuous crack propagation paths, resulting in a relatively high E_p. As stated before, the crack ends before reaching the ASBs (region c), and the ASBs are identified as lamellar austenite (Fig. 8(c1-c3)). Specifically, following crack initiation from the V-notch tip, the extended crack tip is blunted due to the significant volume fraction of the lath-like microstructure. Close examination of the microstructures near the crack path (Fig. 8(a1) and Fig. 8(b1)) revealed that the extensive formation of a lamellar structure deflects the crack propagation. Correspondingly, the BCC phase IPF Z map of region-a and region-b identified the lamellar structures as α′-martensite (Fig. 8(a2) and Fig. 8(b2)).

In summary, The CG and UCG steels exhibit superior E_p values and are characterized by similar crack path profiles and deformed microstructures. The formation of lath-like α′-martensite is responsible for the good crack propagation resistance found in these steels.

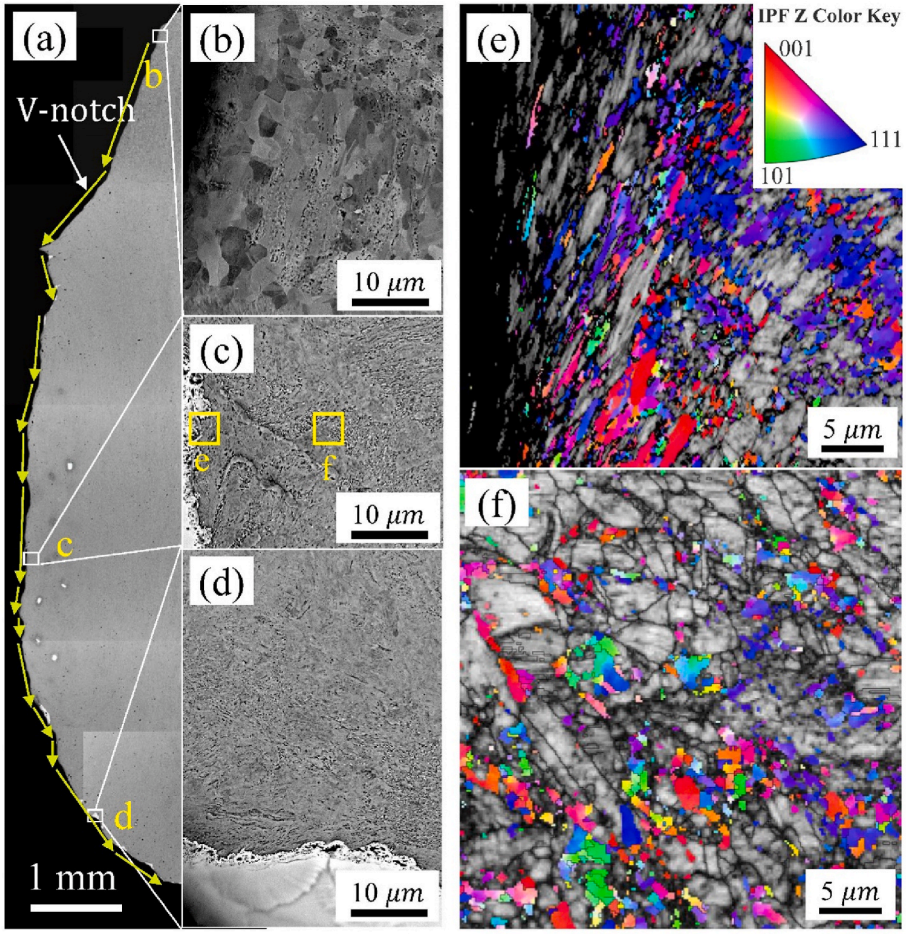

Fig. 5. Crack propagation captured on the UFG specimens. (a) Low-magnification ECCI micrographs of the cross-sectional area of a fractured Charpy impact specimen; (b) deformation structures near the root of the V-notch; (c) and (d) microstructure resulting from dynamic plastic deformation in the plastic-wake regions along the crack path; (e) and (f) colored α′-martensite IPF Z map for the yellow rectangle in (c). (For interpretation of the references to color in this figure legend, the reader is referred to the Web version of this article.)

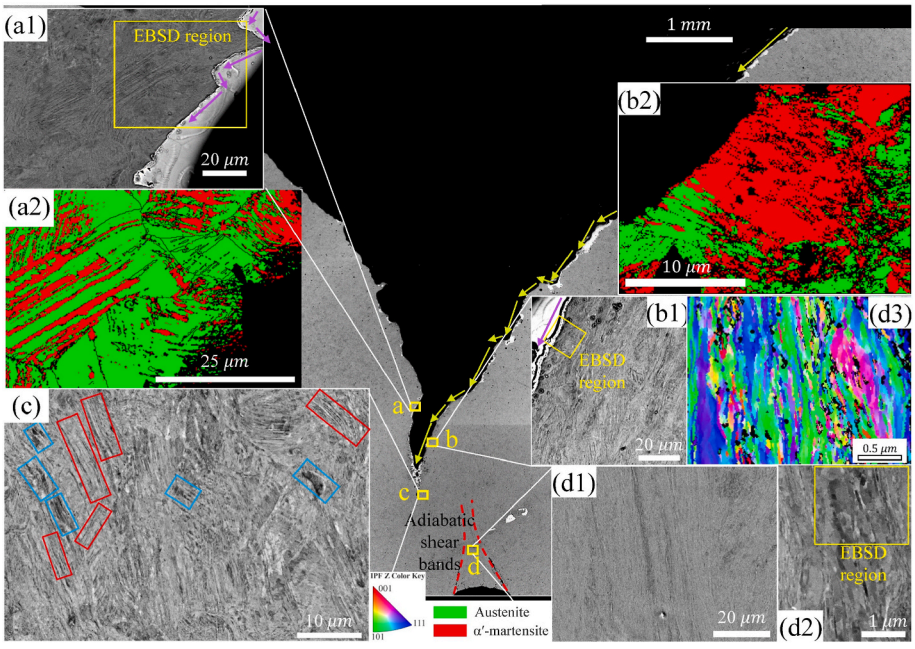

Fig. 6. Crack propagation captured on the FG specimen. The ASBs profile is delineated by the red dotted line. Region a shows the film-like DIMT products formed near the crack edges. Region b shows the globular-like DIMT products formed near the crack edges. (a1) (b1) ECCI map near the crack edges; (a2) (b2) EBSD phase map (red represents α′-martensite; green represents austenite) of the yellow rectangle marked region in (a1) (b1), respectively; (c) Region c shows both the film-like and blocky DIMT products formed near the crack tip; (d1) (d2) Region d shows the refined lamellar structures developed in the ASBs; (d3) IPF Z map of the austenite phase of the yellow rectangle marked region in (d2). (For interpretation of the references to color in this figure legend, the reader is referred to the Web version of this article.)

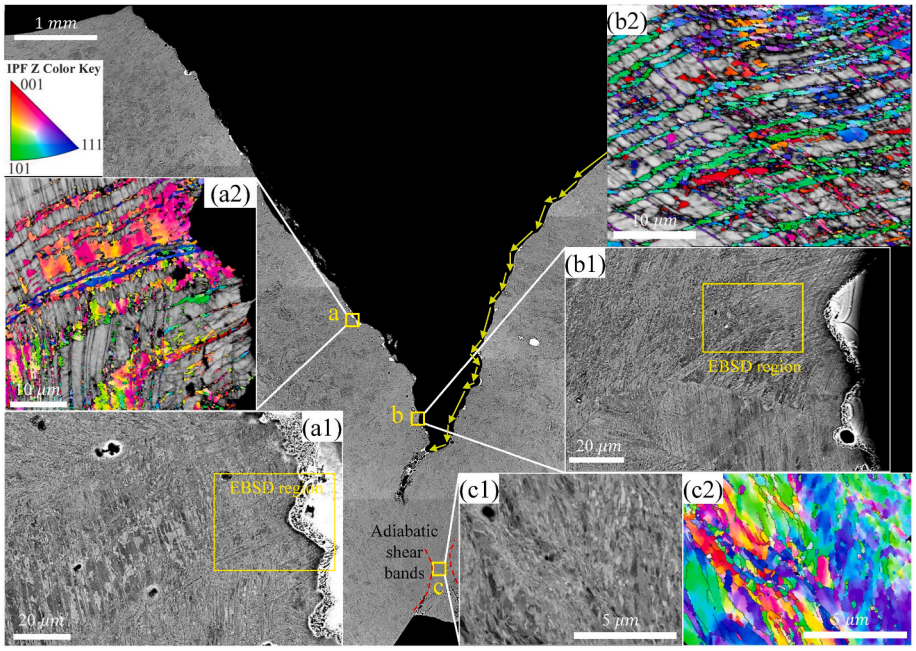

Fig. 7. Crack propagation captured on the CG specimen. The ASBs profile is delineated by the red dotted line. Region a and region b show the film-like DIMT products formed near the crack edges. (a1) (b1) ECCI map near the crack edges; (a2) (b2) IPF Z map of the α′-martensite phase of the yellow rectangle marked region in (a1) (b1), respectively; (c1) Region c shows the refined lamellar structures developed in the ASBs that formed near the ligament end; (c2) IPF Z map of the austenite phase of (c1). (For interpretation of the references to color in this figure legend, the reader is referred to the Web version of this article.)

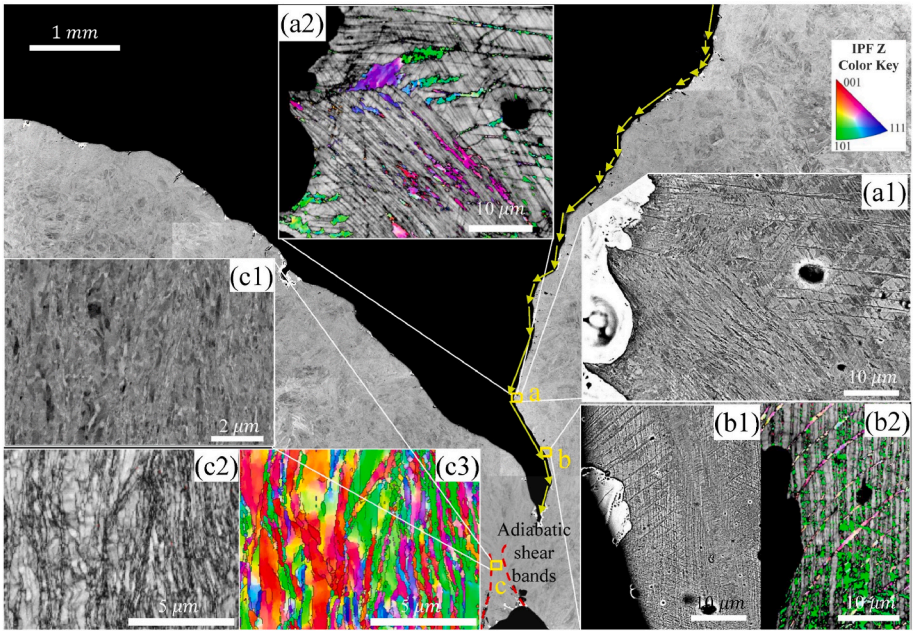

Fig. 8. Crack propagation captured on the UCG specimen, in which the ASBs are delineated by the red dotted line. Region a and region b show the film-like DIMT products formed near the crack edges. (a1) (b1) ECCI map near the crack edges; (a2) (b2) IPF Z map of the α′-martensite phase of the yellow rectangle marked region in (a1) (b1), respectively; (c1) Region-c shows the refined lamellar structures developed in the ASBs that formed near the ligament end; (c2) (c3) band contrast map and IPF Z map of the austenite phase. (For interpretation of the references to color in this figure legend, the reader is referred to the Web version of this article.)

4.2. Size-dependent α′-martensite morphology and its effect on crack propagation

As mentioned in the previous section, the morphology of α′-martensite significantly affects the deflection of propagating cracks and plays a key role in influencing E_p. Therefore, the mechanism underlying the relationship between the AGSs and the morphology of α′-martensite needs to be further clarified, and preferably far away from the cracks to avoid the effect of localized plasticity.

The different morphologies found near the propagating cracks highlight the difference in the nucleation and growth of α′-martensite in steels with various AGSs. Microstructural characterization of UFG, FG, CG, and UCG steels 200 μm away from the notch was carried out, and the results are shown in Fig. 9. The α′-martensite in UFG steel is severely limited by the austenite grain boundaries, leading to the formation of blocky DIMT α′-martensite, as shown in Fig. 9(a and e). As the grain size increases to FG sizes, pronounced twinning formation is observed (Fig. 9 (b and f)), and both TWIP and TRIP behavior occurs in the FG sample. Consistent with the results observed in the fractured FG steel (Fig. 6), both block/film-like α′-martensite exist in FG steel. As the grain sizes further increase to CG sizes, ε-martensite and α′-martensite are formed in the CG steel, and only film-like α′-martensite is found in Fig. 9(c and g). As recognized in previous studies [58], the activation of different deformation mechanisms in austenitic steels is closely related to the stacking fault energy (SFE). The SFE of the UCG steel (24.99 mJ/m^2) is similar to that of the CG steel (25.18 mJ/m^2) according to classical theory [59]. Thus, the martensitic transformation behaviors of the CG and UCG steel are consistent, as shown in Fig. 9. It confirms that both CG

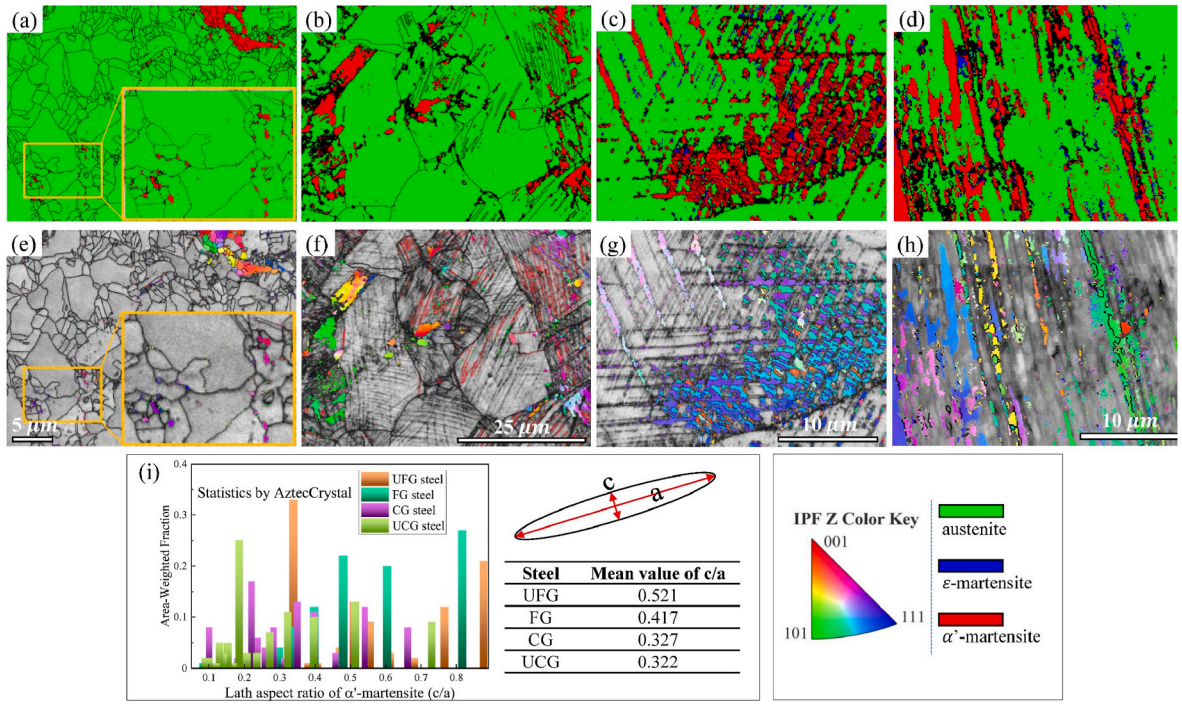

Fig. 9. Microstructural characterization of UFG, FG, CG, and UCG steels 200 μm away from the notch. Phase maps for (a) UFG steel, (b) FG steel, (c) CG steel, and (d) UCG steel, green, blue, red represent the FCC, HCP, and BCC phases; (e) (f) (g) (h) IPF Z maps of the BCC phase, red lines in (f) represent twin boundaries; (i) lath aspect ratio (c/a) distributions for different AGSs. (For interpretation of the references to color in this figure legend, the reader is referred to the Web version of this article.)

and UCG steel consist of austenite, ε-martensite, and lath-like α′-martensite. Furthermore, Fig. 9(i) shows the quantified results of the distributions of the lath aspect ratio (c/a), revealing that the increase in AGSs benefits the formation of lath-like α′-martensite.

Based on the microstructural characterization in Fig. 9, the morphology of α′-martensite and martensitic transformation sequences as a function of the AGSs are schematically shown in Fig. 10. The morphology of α′-martensite is strongly determined by the limitation boundaries. In UFG steel, the formation of blocky α′-martensite is attributed to the absence of deformation bands (both deformation twinning and ε-martensite), which are limited only by austenite grain boundaries in the free growth of α′-martensite. The absence of deformation twinning and ε-martensite can be explained by the relatively high twin nucleation stress (τcritical~598 MPa) and SFE (~33 mJ/m^2), respectively (twin nucleation stress calculated based on the references of Raabe et al. [60]). With the AGSs increasing to FG sizes, the formation of deformation twins provides additional obstacles to martensite growth, and the grain/twin boundaries are responsible for the block/lath-like morphology. In the case of CG/UCG steels, the formation of pre-existing ε-martensite reduces the nucleation barrier of α′-martensite [61], which leads to the preferential nucleation of α′-martensite at ε-martensite, and the growth of α′-martensite is limited by the γ-ε phase boundaries, thus resulting in lath-like α′-martensite. (Note: α′-martensite nucleation behavior in UFG steel based on the references of Wang et al. [62]).

The negative relation between E_p and α′-martensite volume fraction has guided researchers to focus on suppressing the formation of α′-martensite. However, we demonstrate that the effect of the DIMT products on E_p is not only related to the volume fraction of α′-martensite, but also to the morphology of martensite formed during impact loading. The most effective morphology to deflect propagating cracks is α′-martensite with a high aspect ratio, which coincides with the classic theories for crack deflection [63]. Toughening arises primarily from the twist in the crack propagating front between hard and soft phases, as indicated by the deflection profiles shown in Fig. 11. Therefore, a tentative conclusion can be made that the formation of lath-like α′-martensite instead of blocky α′-martensite would weaken the disadvantages of the intrinsically brittle α′-martensite on crack resistance.

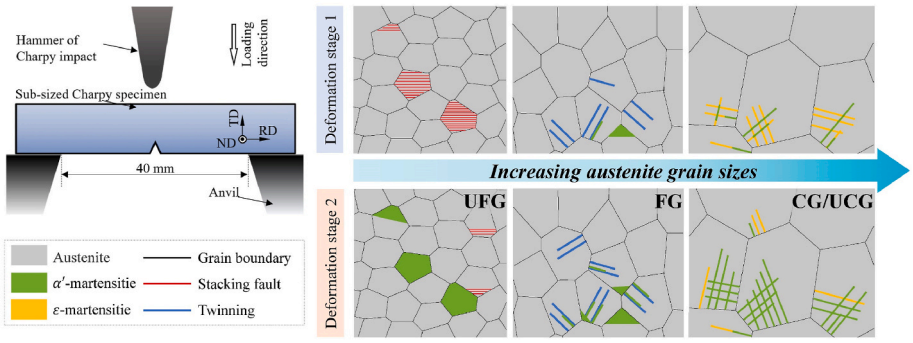

Fig. 10. Schematic of the size-dependent transformation behavior and morphology of α′-martensite during the Charpy impact test.

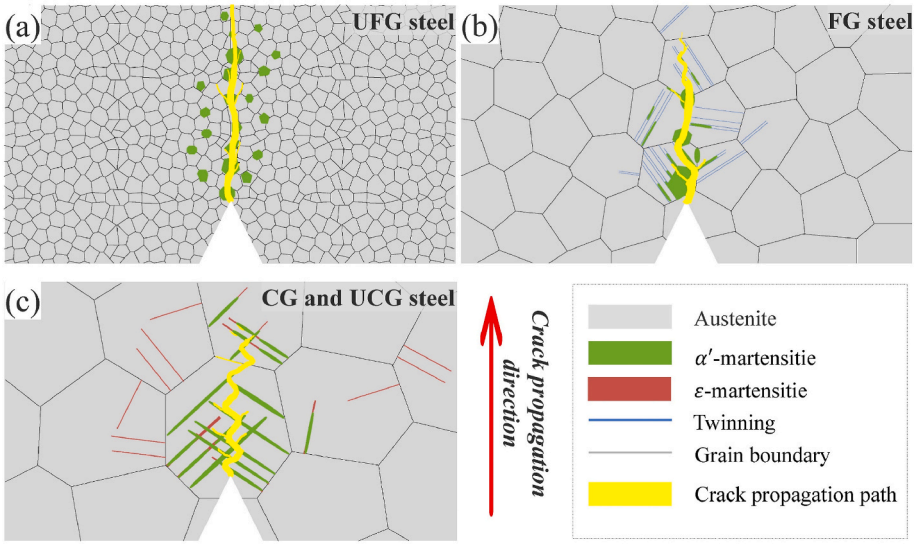

Fig. 11. Schematic diagrams showing the impact of the α′-martensite morphology on the crack propagation path during a Charpy impact test. (a) UFG steel; (b) FG steel; and (c) CG and UCG steel (the green, blue, claret, and yellow colors represent α′-martensite, twinning, ε-martensite, and the crack propagation path, respectively). (For interpretation of the references to color in this figure legend, the reader is referred to the Web version of this article.)

The present study also enables the rational microstructural design of austenitic steels with good crack propagation resistance by controlling the morphology of the formed α′-martensite. It is demonstrated that the reduction of AGS results in the enhancement of yield and tensile strength but deterioration of the impact toughness. While the Hall–Petch effect stands for the improvement of strength, additional alloying methods [64] should be able to control the SFE of austenite to the regime in which the formation of ε-martensite/twins is more favorable than the direct formation of α′-martensite. As a result, the fine-grained austenite matrix can provide the base strength, and the controlled DIMT behavior should lead to the formation of lamellar martensite that can deflect cracks and enhance the impact toughness of the steel. Therefore, the design of austenitic steels with high strength and toughness properties should consider both the strengthening by grain refinement and the toughening by tailored DIMT.

5. Conclusion

This study presents a new approach to minimize the negative effects of the inherent brittleness of α′-martensite without limiting the TRIP effect. In addition, the influence of AGS-controlled α′-martensite morphology on the crack propagation energy of SUS321 is investigated. The following conclusions can be drawn from this investigation:

1. The relationship between the DIMT products and E_p cannot be determined by the α′-martensite volume fraction alone. The morphology of α′-martensite also has a significant effect on the crack propagation energy. It is confirmed that compared to blocky α′-martensite, lath-like α′-martensite can more effectively deflect cracks.
2. The morphology of α′-martensite is controlled by boundary limitations, in which intermediate deformation products (i.e., deformation twins and ε-martensite) are beneficial to the formation of lath-like α′-martensite. If austenite grain boundaries are the only obstacles for martensite growth, blocky α′-martensite will form.
3. For austenitic steels that require both high strength and high toughness, tailoring the SFE of austenite to enhance the twining/ε formation can facilitate the formation of lath-like α′-martensite that promotes strain hardening without deteriorating the crack resistance.

CRediT authorship contribution statement

Minghao Huang: All authors have read and approve this version of the article, Project administration, Funding acquisition, Formal analysis, Supervision, This. **Chenchong Wang:** Data curation, Writing – original draft. **Lingyu Wang:** Funding acquisition, Writing – review & editing. **Jinliang Wang:** Writing – review & editing, not been published or presented elsewhere in part or in entirety and is not under consideration by another. **Anna Mogucheva:** Data curation. **Wei Xu:** Supervision.

Declaration of competing interest

The authors declare that they have no known competing financial interests or personal relationships that could have appeared to influence the work reported in this paper.

Acknowledgements

The research was financially supported by the National Natural Science Foundation of China (No. U1808208, and 51961130389), and International/Regional Cooperation and Exchange Program of NSFC (NSFC-RFBR, No. 52011530032).

References

[1] W.S. Park, S.W. Yoo, M.H. Kim, J.M. Lee, Strain-rate effects on the mechanical behavior of the AISI 300 series of austenitic stainless steel under cryogenic environments, Mater. Des. 31 (2010) 3630–3640, https://doi.org/10.1016/j.matdes.2010.02.041.
[2] H. Wang, J. Zhou, Y. Luo, P. Tang, Y. Chen, Forming of ellipse heads of large-scale Austenitic stainless steel pressure vessel, Procedia Eng. 81 (2014) 837–842, https://doi.org/10.1016/j.proeng.2014.10.085.
[3] M.C. Fonseca, I.N. Bastos, E. Baggio-Saitovitch, D.R. Sánchez, Characterization of oxides of stainless steel UNS S30400 formed in offshore environment, Corrosion Sci. 55 (2012) 34–39, https://doi.org/10.1016/j.corsci.2011.09.029.
[4] J.K. Ren, Q.Y. Chen, J. Chen, Z.Y. Liu, Enhancing strength and cryogenic toughness of high manganese TWIP steel plate by double strengthened structure design, Mater. Sci. Eng., A 786 (2020), https://doi.org/10.1016/j.msea.2020.139397, 139397.1-139397.10.
[5] J. Chen, J.K. Ren, Z.Y. Liu, G.D. Wang, The essential role of niobium in high manganese austenitic steel for application in liquefied natural gas tanks, Mater. Sci. Eng., A 772 (2020), https://doi.org/10.1016/j.msea.2019.138733, 138733.1-138733.8.
[6] R.O. Ritchie, The conflicts between strength and toughness, Nat. Mater. 10 (2011) 817–822, https://doi.org/10.1038/nmat3115.

[7] Z.G. Hu, P. Zhu, J. Meng, Fatigue properties of transformation-induced plasticity and dual-phase steels for auto-body lightweight: experiment, modeling and application, Mater. Des. 31 (2010) 2884–2890, https://doi.org/10.1016/j.matdes.2009.12.034.

[8] X. Li, L. Chen, Y. Zhao, R.D.K. Misra, Influence of manganese content on ε-/α′-martensitic transformation and tensile properties of low-C high-Mn TRIP steels, Mater. Des. 142 (2018) 190–202, https://doi.org/10.1016/j.matdes.2018.01.026.

[9] J. Lu, H. Yu, X.N. Duan, C.H. Song, Study of deformation behavior and microstructural evolution in multiphase steel, 1, Materials 11 (2018) 2285–222285, https://doi.org/10.3390/ma11112285, 15.

[10] Z.H. Cai, H. Ding, R.D.K. Misra, H. Kong, Unique serrated flow dependence of critical stress in a hot-rolled Fe-Mn-Al-C steel, Scripta Mater. 71 (2014) 5–8, https://doi.org/10.1016/j.scriptamat.2013.09.009.

[11] J. Chiang, B. Lawrence, J.D. Boyd, A.K. Pilkey, Effect of microstructure on retained austenite stability and work hardening of TRIP steels, Mater. Sci. Eng. 528 (2011) 4516–4521, https://doi.org/10.1016/j.msea.2011.02.032.

[12] J. Chen, M.Y. Lv, Z.Y. Liu, G.D. Wang, Combination of ductility and toughness by the design of fine ferrite/tempered martensite-austenite microstructure in a low carbon medium manganese alloyed steel plate, Mater. Sci. Eng., A 648 (2015) 51–56, https://doi.org/10.1016/j.msea.2015.09.032.

[13] A. Vinogradov, A. Lazarev, M. Linderov, A. Weidner, H. Biermann, Kinetics of deformation processes in high-alloyed cast transformation-induced plasticity/twinning-induced plasticity steels determined by acoustic emission and scanning electron microscopy: influence of austenite stability on deformation mechanisms, Acta Mater. 61 (2013) 2434–2449, https://doi.org/10.1016/j.actamat.2013.01.016.

[14] M.C. Jo, M.C. Jo, A. Zargaran, S.S. Sohn, S. Lee, Effects of Al addition on tensile properties of partially recrystallized austenitic TRIP/TWIP steels, Mater. Sci. Eng., A 806 (2021), https://doi.org/10.1016/j.msea.2021.140823, 140823.1-140823.9.

[15] C. Quitzke, C. Schrder, C. Ullrich, M. Mandel, M. Wendler, Evaluation of strain-induced martensite formation and mechanical properties in N-alloyed austenitic stainless steels by in situ tensile tests, Mater. Sci. Eng., A 808 (2021), https://doi.org/10.1016/j.msea.2021.140930, 140930.1-140930.12.

[16] A. Nazari, J.A. Mohandesi, M.H. Vishkasogheh, M. Abedi, Simulation of impact energy in functionally graded steels, Comput. Mater. Sci. 50 (2011) 1187–1196, https://doi.org/10.1016/j.commatsci.2010.11.019.

[17] M. Kang, H. Kim, S. Lee, S.Y. Shin, Effects of dynamic strain hardening exponent on abnormal cleavage fracture occurring during drop weight tear test of API X70 and X80 linepipe steels, Metall. Mater. Trans. 45 (2014) 682–697, https://doi.org/10.1007/s11661-013-2046-7.

[18] B. Hwang, T.H. Lee, S.J. Kim, Effects of deformation-induced martensite and grain size on ductile-to-brittle transition behavior of austenitic 18Cr-10Mn-N stainless steels, Met. Mater. Int. 16 (2010) 905–911, https://doi.org/10.1007/s12540-010-1208-z.

[19] B. Avishan, S. Yazdani, S.H. Nedjad, Toughness variations in nanostructured bainitic steels, Mater. Sci. Eng., A 548 (2012) 106–111, https://doi.org/10.1016/j.msea.2012.03.098.

[20] H. Kim, J. Park, J.E. Jung, S.S. Sohn, S. Lee, Interpretation of cryogenic-temperature Charpy fracture initiation and propagation energies by microstructural evolution occurring during dynamic compressive test of austenitic Fe–(0.4,1.0)C–18Mn steels, Mater. Sci. Eng. 641 (2015) 340–347, https://doi.org/10.1016/j.msea.2015.05.095.

[21] S.G. Lee, B. Kim, M.C. Jo, K.M. Kim, J. Lee, J. Bae, B.J. Lee, S.S. Sohn, S. Lee, Effects of Cr addition on Charpy impact energy in austenitic 0.45C-24Mn-(0,3,6)Cr steels, J. Mater. Sci. Technol. 50 (2020) 21–30, https://doi.org/10.1016/j.jmst.2019.12.032.

[22] B. Hwang, T.H. Lee, S.J. Park, C.S. Oh, S.J. Kim, Correlation of austenite stability and ductile-to-brittle transition behavior of high-nitrogen 18Cr–10Mn austenitic steels, Mater. Sci. Eng., A 528 (2011) 7257–7266, https://doi.org/10.1016/j.msea.2011.06.025.

[23] L.C.D. Fielding, N.G. Jones, J. Walsh, S.V. Boxel, M.S. Blackmur, P.D. Lee, P. J. Withers, H.J. Stone, H.K.D.H. Bhadeshia, Synchrotron analysis of toughness anomalies in nanostructured bainite, Acta Mater. 105 (2016) 52–58, https://doi.org/10.1016/j.actamat.2015.11.029.

[24] J. Kang, F.C. Zhang, X.Y. Long, B. Lv, Low cycle fatigue behavior in a medium-carbon carbide-free bainitic steel, Mater. Sci. Eng. 666 (2016) 88–93, https://doi.org/10.1016/j.msea.2016.03.077.

[25] J. Kang, C. Wang, G.D. Wang, Microstructural characteristics and impact fracture behavior of a high-strength low-alloy steel treated by intercritical heat treatment, Mater. Sci. Eng., A 553 (2012) 96–104, https://doi.org/10.1016/j.msea.2012.05.098.

[26] H. Kim, Y. Ha, K.H. Kwon, M. Kang, N.J. Kim, S. Lee, Interpretation of cryogenic-temperature Charpy impact toughness by microstructural evolution of dynamically compressed specimens in austenitic 0.4C-(22-26)Mn steels, Acta Mater. 87 (2015) 332–343, https://doi.org/10.1016/j.actamat.2014.11.027.

[27] J. Lee, S.S. Sohn, S. Hong, B.C. Suh, S.K. Kim, B.J. Lee, N.J. Kim, S. Lee, Effects of Mn addition on tensile and Charpy impact properties in austenitic Fe-Mn-C-Al-based steels for cryogenic applications, Metall. Mater. Trans. 45 (2014) 5419–5430, https://doi.org/10.1007/s11661-014-2513-9.

[28] S.S. Sohn, S. Hong, J. Lee, B.C. Suh, S.K. Kim, B.J. Lee, N.J. Kim, S. Lee, Effects of Mn and Al contents on cryogenic-temperature tensile and Charpy impact properties in four austenitic high-Mn steels, Acta Mater. 100 (2015) 39–52, https://doi.org/10.1016/j.actamat.2015.08.027.

[29] M.X. Zhang, P.M. Kelly, Stress-induced martensitic transformation and impact toughness of cast irons and high-carbon Fe-Ni-C steel, Metall. Mater. Trans. 32 (2001) 2695–2708, https://doi.org/10.1007/s11661-001-1022-9.

[30] M.X. Zhang, P.M. Kelly, Relationship between stress-induced martensitic transformation and impact toughness in low carbon austenitic steels, J. Mater. Sci. 37 (2002) 3603–3613, https://doi.org/10.1023/A:1016544821646.

[31] S.D. Antolovich, Fracture toughness and strain-induced phase transformations, Trans. Metallur. Soc. AIME 242 (1968) 2371–2373.

[32] Y. Li, Y. Lu, W. Li, M. Khedr, H. Liu, X. Jin, Hierarchical microstructure design of a bimodal grained twinning-induced plasticity steel with excellent cryogenic mechanical properties, Acta Mater. 158 (2018) 79–94, https://doi.org/10.1016/j.actamat.2018.06.019.

[33] Z.H. Lai, Y.H. Sun, Y.T. Lin, J.F. Tu, H.W. Yen, Mechanism of twinning induced plasticity in austenitic lightweight steel driven by compositional complexity, Acta Mater. 210 (2021), https://doi.org/10.1016/j.actamat.2021.116814, 116814.1-116814.12.

[34] A.A. Tiamiyu, A.G. Odeshi, J.A. Szpunar, Multiple strengthening sources and adiabatic shear banding during high strain-rate deformation of AISI 321 austenitic stainless steel: effects of grain size and strain rate, Mater. Sci. Eng., A 711 (2018) 233–249, https://doi.org/10.1016/j.msea.2017.11.045.

[35] M.H. Huang, L.Y. Wang, C.C. Wang, A. Mongucheva, W. Xu, Characterization of deformation-induced martensite with various AGSs upon Charpy impact loading and correlation with transformation mechanisms, Mater. Char. 184 (2022) 199–206, https://doi.org/10.1016/j.matchar.2021.111704.

[36] H. Kwon, P. Sathiyamoorthi, G.K. Karthik, P. Asghari-Rad, A. Zargaran, H.S. Do, B. J. Lee, H. Kato, H.S. Kim, 2.3 GPa cryogenic strength through thermal-induced and deformation-induced body-centered cubic martensite in a novel ferrous medium entropy alloy, Scripta Mater. 204 (2021), 114157, https://doi.org/10.1016/j.scriptamat.2021.114157.

[37] M.J. Sohrabi, M. Naghizadeh, H. Mirzadeh, Deformation-induced martensite in austenitic stainless steels: a review, Arch. Civ. Mech. Eng. 20 (2020) 1539, https://doi.org/10.1007/s43452-020-00130-1.

[38] S. Kheiri, H. Mirzadeh, M. Naghizadeh, Tailoring the microstructure and mechanical properties of AISI 316L austenitic stainless steel via cold rolling and reversion annealing, Mater. Sci. Eng., A 759 (2019) 90–96, https://doi.org/10.1016/j.msea.2019.05.028.

[39] J.X. Zhang, Y.M. He, Y.H. Wang, Y.F. Wang, T.S. Wang, Influence of annealing temperature on microstructure, tensile properties and tensile deformation mechanism of metastable austenitic stainless steel repetitively cold-rolled and annealed, Materialia 8 (2019), 100455, https://doi.org/10.1016/j.mtla.2019.100455.

[40] Z.B. Dai, H. Chen, R. Ding, Q. Lu, C. Zhang, Z.G. Yang, S.V.D. Zwaag, Fundamentals and application of solid-state phase transformations for advanced high strength steels containing metastable retained austenite, Mater. Sci. Eng. R Rep. 143 (2021), 100590, https://doi.org/10.1016/j.mser.2020.100590.

[41] M. Soleimani, A. Kalhor, H. Mirzadeh, Transformation-induced plasticity (TRIP) in advanced steels: a review, Mater. Sci. Eng. 795 (2020), 140023, https://doi.org/10.1016/j.msea.2020.140023.

[42] D. Liu, B. Cheng, Y. Chen, Strengthening and toughening of a heavy plate steel for shipbuilding with yield strength of approximately 690 MPa, Metall. Mater. Trans. 44 (2013) 440–455, https://doi.org/10.1007/s11661-012-1389-9.

[43] J.K. Ren, D.S. Mao, Y. Gao, J. Chen, Z.Y. Liu, High carbon alloyed design of a hot-rolled high-Mn austenitic steel with excellent mechanical properties for cryogenic application, Mater. Sci. Eng., A 827 (2021), 141959, https://doi.org/10.1016/j.msea.2021.141959.

[44] T. Hanamura, H. Qiu, Ultra-Fine-Grained Steel: Relationship between Grain Size and Impact Properties, Analysis of Fracture Toughness Mechanism in Ultra-fine-grained Steels, 2014, pp. 22–47, https://doi.org/10.1007/978-4-431-54499-9_3.

[45] J.R. Tarpani, D. Spinelli, Grain size effects in the Charpy impact energy of a thermally embrittled RPV steel, J. Mater. Sci. 38 (2007) 1493–1498, https://doi.org/10.1023/A:1022920514474.

[46] H. H Wang, L. Meng, Q. Luo, C. Sun, G.Q. Li, X.L. Wan, Superior cryogenic toughness of high-Mn austenitic steel by welding thermal cycles: the role of grain boundary evolution, Mater. Sci. Eng., A 788 (2020), 139573, https://doi.org/10.1016/j.msea.2020.139573.

[47] J. Chen, F.T. Dong, H.L. Jiang, Z.Y. Liu, G.D. Wang, Influence of final rolling temperature on microstructure and mechanical properties in a hot-rolled TWIP steel for cryogenic application, Mater. Sci. Eng., A 724 (2018) 330–334, https://doi.org/10.1016/j.msea.2018.03.111.

[48] J. Chen, F.T. Dong, Z.Y. Liu, G.D. Wang, Grain size dependence of twinning behaviors and resultant cryogenic impact toughness in high manganese austenitic steel, J. Mater. Res. Technol. 10 (2021) 175–187, https://doi.org/10.1016/j.jmrt.2020.12.030.

[49] J.K. Ren, Q.Y. Chen, J. Chen, Z.Y. Liu, Enhancing strength and cryogenic toughness of high manganese TWIP steel plate by double strengthened structure design, Mater. Sci. Eng., A 786 (2020), 139397, https://doi.org/10.1016/j.msea.2020.139397.

[50] Y.S. Jung, Y.K. Lee, D.K. Matlock, M.C. Mataya, Effect of grain size on strain-induced martensitic transformation start temperature in an ultrafine grained metastable austenitic steel, Met. Mater. Int. 17 (2011) 553–556, https://doi.org/10.1007/s12540-011-0804-x.

[51] A.D. Schino, M. Barteri, J.M. Kenny, Effects of grain size on the properties of a low nickel austenitic stainless steel, J. Mater. Sci. 38 (2003) 4725–4733, https://doi.org/10.1023/A:1027470917858.

[52] J. Han, A.K. Silva, D. Ponge, D. Raabe, S.M. Lee, Y.K. Lee, S.I. Lee, B. Hwang, The effects of prior austenite grain boundaries and microstructural morphology on the

impact toughness of intercritically annealed medium Mn steel, Acta Mater. 122 (2017) 199–206, https://doi.org/10.1016/j.actamat.2016.09.048.
[53] C. Buirette, J. Huez, N. Gey, A. Vassel, E. Andrieu, Study of crack propagation mechanisms during Charpy impact toughness tests on both equiaxed and lamellar microstructures of Ti-6Al-4V titanium alloy, Mater. Sci. Eng., A 618 (2014) 546–557, https://doi.org/10.1016/j.msea.2014.09.048.
[54] J. Xu, W. Zeng, Y. Zhao, Z. Jia, Effect of microstructure evolution of the lamellar alpha on impact toughness in a two-phase titanium alloy, Mater. Sci. Eng. 676 (2016) 434–440, https://doi.org/10.1016/j.msea.2016.09.017.
[55] X.J. Tian, S.Q. Zhang, A. Li, H.M. Wang, Effect of annealing temperature on the notch impact toughness of a laser melting deposited titanium alloy Ti-4Al-1.5Mn, Mater. Sci. Eng. 527 (2010) 1821–1827, https://doi.org/10.1016/j.msea.2009.11.014.
[56] C. Wu, Y. Zhao, S. Huang, L. Lei, Q. Zhao, Q. Sun, L. Zhou, Microstructure tailoring and impact toughness of a newly developed high strength Ti-5Al-3Mo-3V-2Cr-2Zr-1Nb-1Fe alloy, Mater. Char. 175 (2021) 111103.1–111103.12, https://doi.org/10.1016/j.matchar.2021.111103.
[57] L. Liu, Q. Yu, Z. Wang, J. Ell, M.X. Huang, R.O. Ritchie, Making ultrastrong steel tough by grain-boundary delamination, Science 368 (2020) 1347–1352, https://doi.org/10.1126/science.aba9413.
[58] O.A. Zambrano, A general perspective of Fe-Mn-Al-C steels, J. Mater. Sci. 53 (2017) 14003–14062, https://doi.org/10.1007/s10853-018-2551-6.
[59] Y.K. Lee, C. Choi, Driving force for γ→ε martensitic transformation and stacking fault energy of γ in Fe-Mn binary system, Metall. Mater. Trans. 31 (2000) 355–360, https://doi.org/10.1007/s11661-000-0271-3.
[60] I. Gutierrez-Urrutia, S. Zaefferer, D. Raabe, The effect of grain size and grain orientation on deformation twinning in a Fe-22 wt.% Mn-0.6 wt.% C TWIP steel[J], Mater. Sci. Eng. 527 (2010) 3552–3560, https://doi.org/10.1016/j.msea.2010.02.041.
[61] M. Huang, J. Yuan, J. Wang, L. Wang, A. Mogucheva, W. Xu, Role of martensitic transformation sequences on deformation-induced martensitic transformation at high strain rates: a quasi in-situ study, Mater. Sci. Eng., A 831 (2022), https://doi.org/10.1016/j.msea.2021.142319, 142319.1-142319.10.
[62] M.M. Wang, C.C. Tasan, D. Ponge, A. Kostka, D. Raabe, Smaller is less stable: size effects on twinning vs. transformation of reverted austenite in TRIP-maraging steels, Acta Mater. 79 (2014) 268–281, https://doi.org/10.1016/j.actamat.2014.07.020.
[63] K.T. Faber, A.G. Evans, Crack deflection process-I. Theory, Acta Metall. 31 (1983) 565–576, https://doi.org/10.1016/0001-6160(83)90046-9.
[64] Q. Luo, H.H. Wang, G.Q. Li, C. Sun, D.H. Li, X.L. Wan, On mechanical properties of novel high-Mn cryogenic steel in terms of SFE and microstructural evolution, Mater. Sci. Eng., A 753 (2019) 91–98, https://doi.org/10.1016/j.msea.2019.02.093.